

Accepted Manuscript

Numerical study of the thermal performance of the CERN Linac3 ion source miniature oven

C. Fichera, F. Carra, D. Küchler, V. Toivanen

PII: S0168-9002(18)30641-7
DOI: <https://doi.org/10.1016/j.nima.2018.05.036>
Reference: NIMA 60820

To appear in: *Nuclear Inst. and Methods in Physics Research, A*

Received date: 8 January 2018
Revised date: 26 March 2018
Accepted date: 15 May 2018

Please cite this article as: C. Fichera, F. Carra, D. Küchler, V. Toivanen, Numerical study of the thermal performance of the CERN Linac3 ion source miniature oven, *Nuclear Inst. and Methods in Physics Research, A* (2018), <https://doi.org/10.1016/j.nima.2018.05.036>

This is a PDF file of an unedited manuscript that has been accepted for publication. As a service to our customers we are providing this early version of the manuscript. The manuscript will undergo copyediting, typesetting, and review of the resulting proof before it is published in its final form. Please note that during the production process errors may be discovered which could affect the content, and all legal disclaimers that apply to the journal pertain.



1 Numerical study of the thermal performance of the CERN Linac3 ion 2 source miniature oven

3 C. Fichera¹, F. Carra¹, D. K uchler¹, V. Toivanen²

4 ¹European Organization for Nuclear Research (CERN), Geneva, Switzerland

5 ²Grand Acc el rateur National d'Ions Lourds (GANIL), Caen Cedex, France

6

7

8

9 Abstract

10 The Linac3 ion source at CERN produces lead ion beams by the vaporization of solid samples
11 inside the internal ovens and the consequent ionization of the evaporated material in the
12 plasma. The geometry, materials and surface state of the oven elements are critical parameters
13 influencing the oven temperature characteristics and consequently the evaporation properties
14 and the ion source performance. A dedicated test stand was assembled and a finite element
15 approach is proposed to evaluate the thermal response of the system at increasing heating
16 powers. Comparisons between the simulation results and experimental measurements are
17 given in order to validate the numerical model. Radiation was found to be the main heat
18 transfer mechanism governing the system. Based on the obtained results, improvements to the
19 existing setup are analysed.

20

21 **Keywords:** Linear accelerator; accelerator equipment design; CERN; finite elements method;
22 numerical thermal analysis; heat transfer.

23

24 1. Introduction

25 In the framework of the High Luminosity project of the Large Hadron Collider
26 (HL-LHC), all the LHC injectors are undergoing an extensive upgrade program, named LHC
27 Injector Upgrade (LIU) [1]. The first link of the heavy ion accelerator chain is represented by
28 the Linac3 linear accelerator, Fig. 1, operating since 1994 [2]. As a part of the Linac3
29 upgrades, several activities involve the GTS-LHC Electron Cyclotron Resonance ion source
30 (ECR), which produces the primary heavy ion beams [3]. The major efforts focus on the
31 GTS-LHC extraction region, the double frequency plasma heating combined with afterglow
32 operation [4] and the oven studies for metal ion beam production [5]. Concerning the oven
33 studies, the lead ion beams delivered by the Linac3 are produced with the ECRIS using
34 resistively-heated miniature ovens. Since the oven performance is related to the temperature
35 distribution, a dedicated off-line test stand was built with the capability of measuring the oven
36 temperatures and a numerical thermal model was developed to complement the measurements
37 and evaluate the criticality of the several parameters involved. The application of the finite
38 element method in the study of an ion source is a novelty in the accelerator community. In the
39 following chapters the features of the advanced numerical method developed using the
40 ANSYS Workbench finite element code [6] are described in detail, focusing the attention on
41 the loading conditions, the material data and the assumptions adopted. The theoretical
42 principles of the heat exchange are recalled to justify the assumptions taken. A benchmarking
43 is performed between the numerical results and the experimental data in order to validate the
44 numerical model. Finally, some recommendations are given for future and similar

45 technologies and new solutions are proposed to improve the performance and service life of
 46 the source.

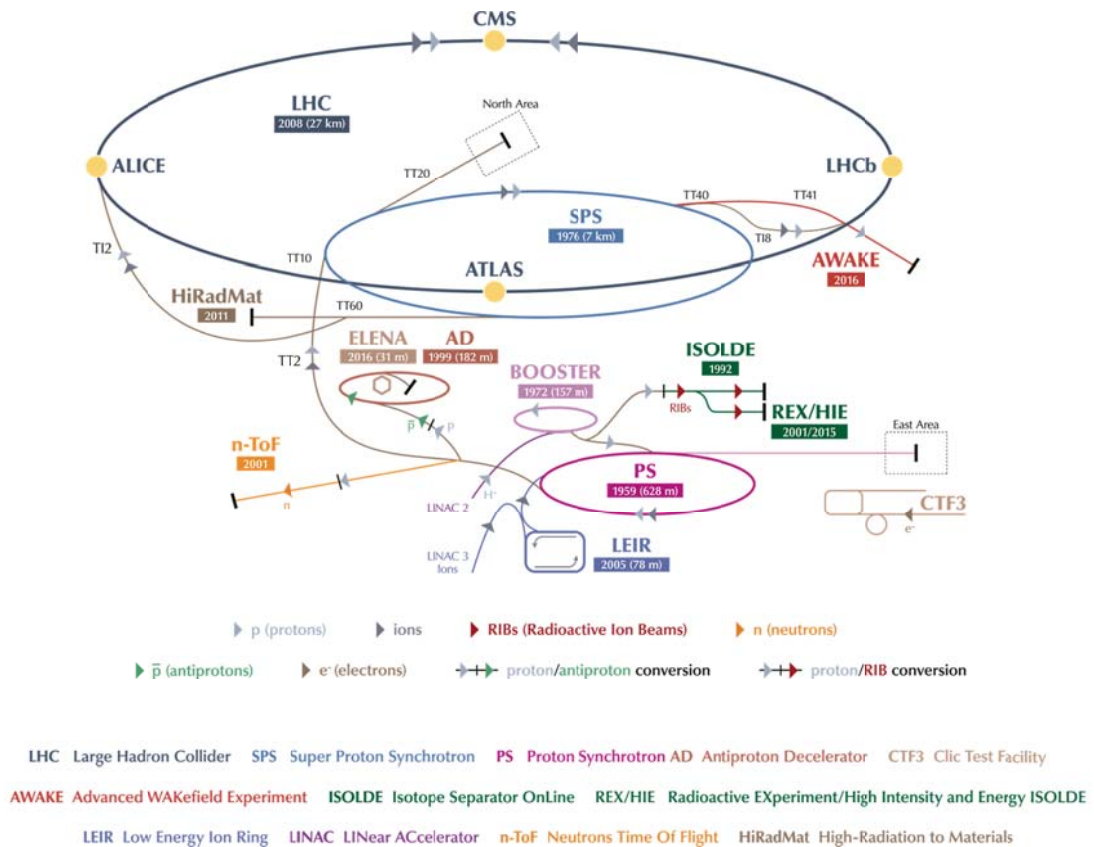
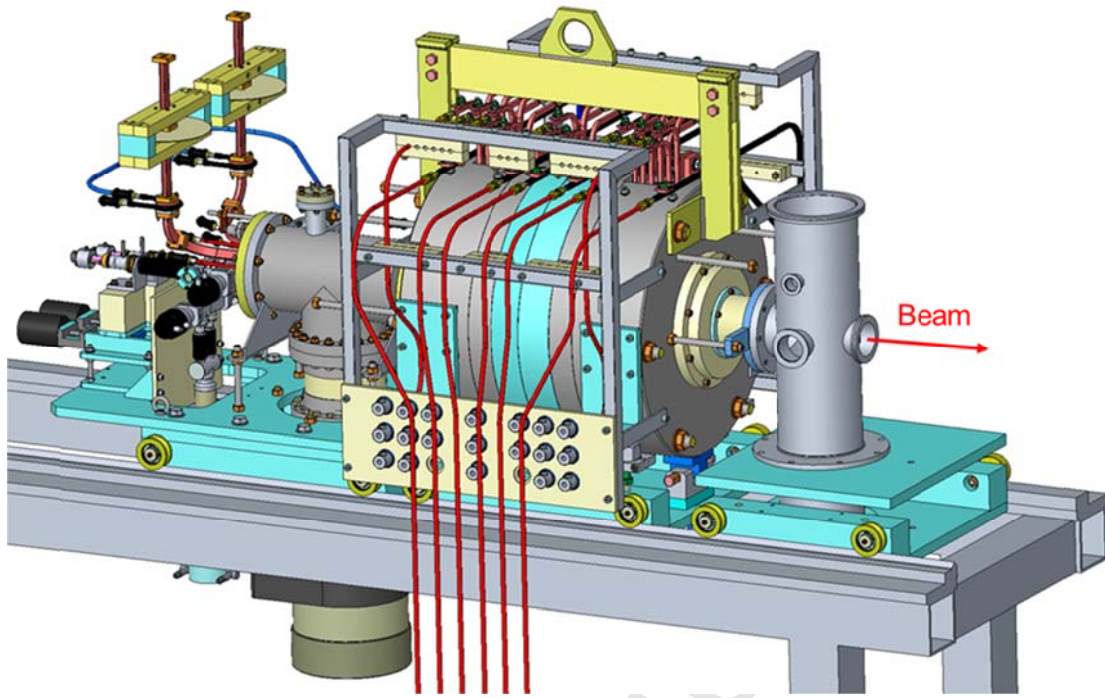


Figure 1 The CERN accelerator complex

50 2. Component description

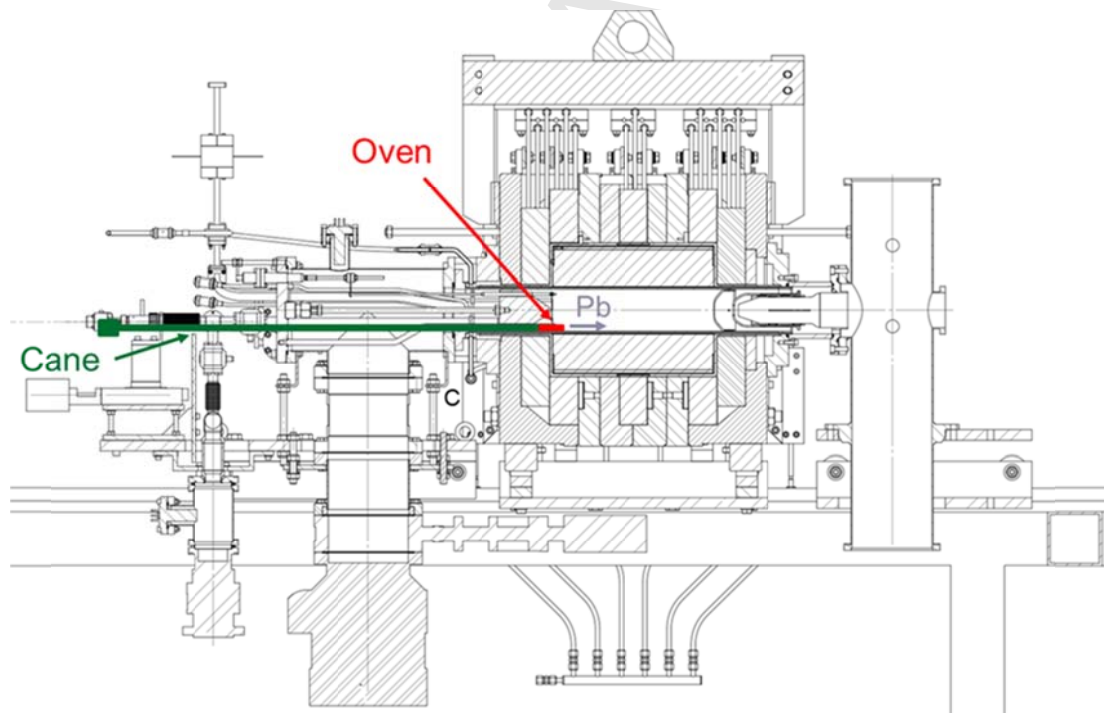
51 The GTS-LHC 14.5 GHz ECR ion source, [Fig. 2](#), provides highly-charged heavy ion
 52 beams, predominantly lead, for the CERN experiments. The beam is generated from solid
 53 material evaporated in the ion source plasma chamber with resistively-heated ovens. The oven
 54 consists of a long vacuum-sealed stainless steel cane¹, which contains a copper wire
 55 connected, at the end of the cane, to a tantalum heating filament wound around the crucible.
 56 The cane allows the axial insertion of the oven through the ion source injection plug, [Fig. 3](#).
 57 The crucible is made of alumina, as well as the filament support and insulator. Finally, the
 58 crucible is positioned inside a tantalum shell which is connected to the cane, [Fig. 4](#). The outer
 59 diameter of the oven is 14 mm and the total length, including the cane, is 870 mm, while the
 60 diameter of the tantalum filament is 0.45 mm. At the tip of the oven, two holes with a
 61 diameter of 1.5 mm and 5.5 mm in the crucible and the tantalum cover, respectively, allow the
 evaporation of neutral atomic lead. The system can be dismantled to refill the crucible.

¹ This designation is technically used to identify the cylindrical shell containing the current lead.



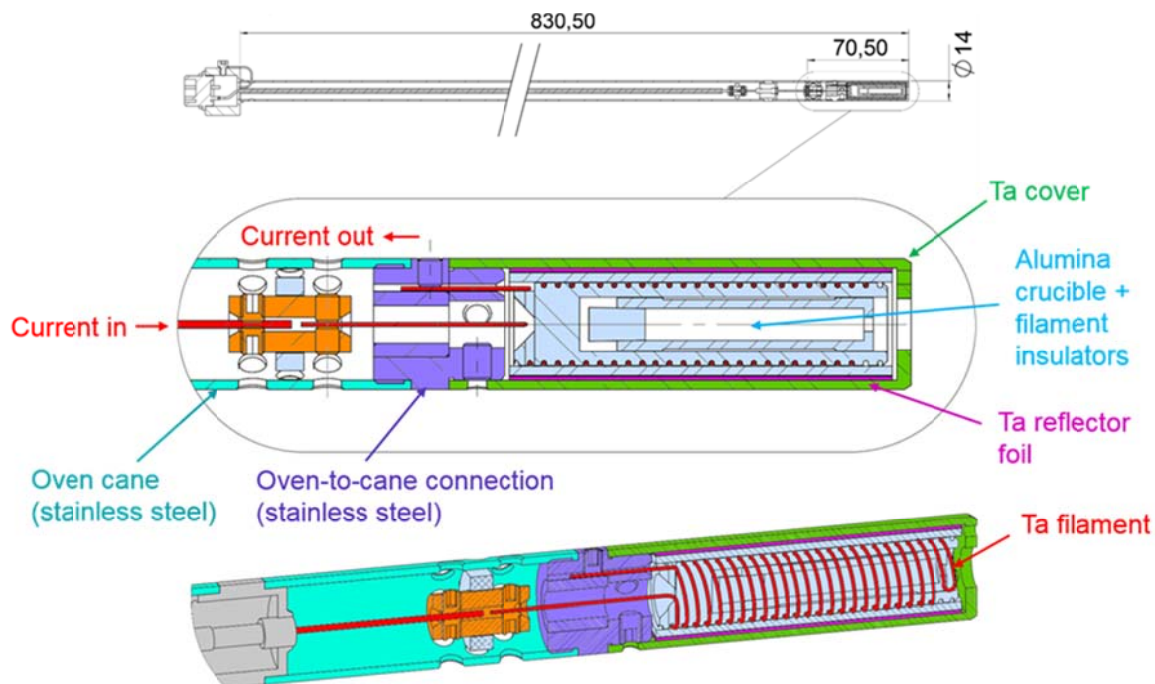
62

63 Figure 2 Linac3 GTS-LHC ECR Ion Source (for clarity, the extraction vacuum pumps are
64 not shown).



65

66 Figure 3 Cross section of the Linac3 GTS-LHC ECR Ion Source.



67

68

Figure 4 GTS-LHC resistively-heated miniature oven.

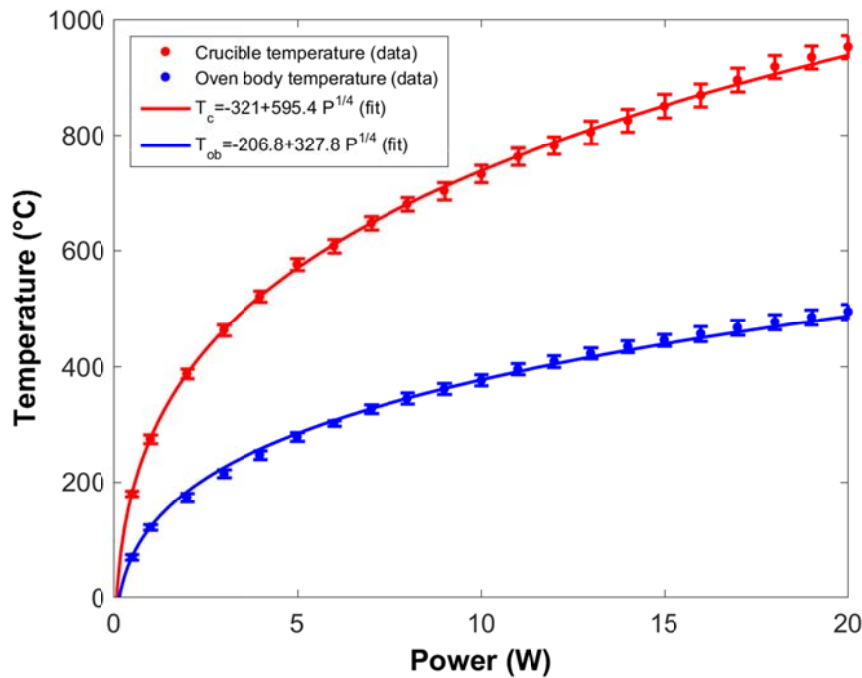
69 The crucible refilling is required every 2-3 operating weeks due to degrading beam
 70 performance. In some instances, the beam production is interrupted by blockage of the oven
 71 tip, either by formation of lead oxide or droplets of metallic lead [5]. These issues could be
 72 provoked by non-homogeneous temperature distribution along the crucible or temperature
 73 gradients in the neutral lead exit zone. In that sense, the thermal analysis of the system should
 74 provide further details about the oven behaviour.

75 3. Experimental measurements

76 A dedicated off-line test stand was built at CERN for monitoring the behaviour of the
 77 oven during the heating process, acquiring the most relevant physical quantities, such as the
 78 temperature in fixed points and the lead evaporation rates [5]. In particular, the oven was
 79 equipped with vacuum-grade thermocouples in order to measure the internal and external
 80 temperature. The thermocouple measuring the temperature inside the oven was secured to a
 81 copper pin 23 mm long with a diameter of 3 mm. The copper pin is inserted inside the
 82 alumina crucible and replaces the lead in order to perform measurements up to 1000 °C. On
 83 top of that, an additional thermocouple was attached to the outside surface of the tantalum
 84 shell, placed at the axial location corresponding to the centre of the crucible. In this case, the
 85 thermocouple was fixed with a clamping system made of a stainless steel ring and a central
 86 screw, as shown in Fig. 5. In normal operation, the oven heating power is limited to 20 W. In
 87 Fig. 6, the experimental temperatures are reported as a function of the heating power in
 88 steady-state conditions.



89
90 Figure 5 *left)* Stainless steel holder ring for thermocouple installation and *right)* setup for
91 oven temperature measurements.



92
93 Figure 6 Measured temperature vs. oven power: crucible (*red solid line*) and oven body
94 temperature (*blue solid line*).

95 For the production of lead beams, the oven is normally operated with power levels
96 above 6 W. One can observe that the measured oven temperatures follow a $T \propto P^{1/4}$
97 relationship, where P is the power to the oven. Usually, this behaviour is typical of thermal
98 radiation problems, as will be shown in the following section.

99 4. Heat transfer mechanisms

100 The heat transfer mechanisms governing the system under study were examined in
101 detail to determine the most appropriate material parameters and boundary conditions for the
102 thermal analysis. The conservation of energy specifies that net exchange of the energy of a
103 system is always equal to the net transfer of energy across the boundary system as heat and
104 work; applying this to a differential volume and considering the time variable t , the heat
105 equation assumes the following differential form:

$$106 \quad \rho c_p \frac{\partial T}{\partial t} - k \nabla^2 T = Q \quad (1)$$

107 The first term represents the transient part in which the energy is released or stored,
 108 where c_p is the specific heat capacity and ρ is the density. The second term is the temperature
 109 variation along the component, where k is the thermal conductivity and ∇^2 the Laplace
 110 operator, $\left(\frac{\partial^2 T}{\partial x^2} + \frac{\partial^2 T}{\partial y^2} + \frac{\partial^2 T}{\partial z^2}\right)$ in Cartesian coordinates, while Q is the internal heat generation
 111 rate per unit volume. The material properties are a function of the temperature. The heat
 112 equation is a partial differential equation that describes the distribution of heat (or variation of
 113 temperature) in a given region over time. In some cases, exact solutions of the equation are
 114 available; in other cases the equation must be solved numerically using computational
 115 methods. In a steady-state case, the thermal gradient is constant with time, $\frac{\partial T}{\partial t} = 0$ and the
 116 equation (1) simplifies to:

$$117 \quad -k\nabla^2 T = Q \quad (2)$$

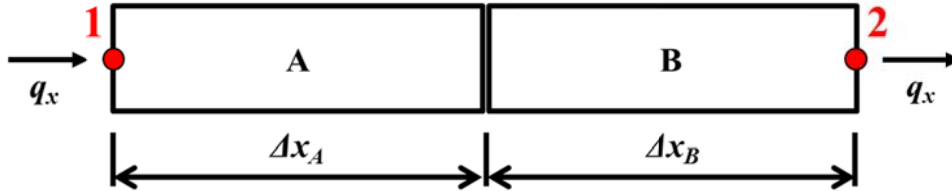
118 In this work it is assumed that, both in the measurements and in the simulations, the
 119 steady-state condition is reached and (2) applies.

120 The exchange of energy in the system is regulated by the combination of three
 121 fundamental modes of heat transfer: conduction, convection and radiation.

122 4.1 Conduction

123 In the heat exchange by conduction, the internal heat transfer occurs between two points
 124 of the same body or two bodies in contact. The temperature gradient on a body in steady-state
 125 conditions follows the definition in (2). In the case of two bodies in contact, such as A and B
 126 in Fig. 7, the thermal flux between two points is:

$$127 \quad q_x = -\frac{T_1 - T_2}{\frac{\Delta x_A}{k_A \cdot S} + \frac{1}{h_c \cdot S} + \frac{\Delta x_B}{k_B \cdot S}} \quad (3)$$



128

129 Figure 7 Thermal flux between two solids in contact.

130 where S is the contact area, x the orthogonal direction, Δx_A and Δx_B the distances of the
 131 measuring points 1 and 2 from the interface. The thermal flux thus depends on the geometry
 132 of the bodies, on their thermal conductivity and on the coefficient h_c , which is called thermal
 133 contact conductance. This parameter is of paramount importance in the case of heat exchange
 134 between two good conductors, where most of the temperature gradient is often generated at
 135 the interface. The contact conductance is influenced by many factors, the contact pressure
 136 being the most important. The influence of the contact pressure on the thermal contact
 137 conductance has been widely discussed by many authors [7,8] and their relationship is
 138 typically expressed as follows:

$$139 \quad h_c = 1.25k_s \left(\frac{m}{\sigma}\right) \left(\frac{P}{H_e}\right)^{0.95} \quad (4)$$

140 where k_s is the harmonic mean of the thermal conductivities, σ is the roughness and m
 141 the related surface slope, while P is the contact pressure and H_e the effective elastic

142 micro-hardness. Considering the system under study, most of the bodies in contact have a
 143 very low contact pressure, comparable to that generated by their deadweight, and the
 144 contribution of thermal conduction in the heat exchange between bodies in contact is expected
 145 to be negligible with respect to the heat exchanged by radiation (see section 6.3).

146 4.2 Convection

147 Convection is the thermal exchange between a body and a surrounding fluid in motion.
 148 The basic relationship for the convection heat transfer is defined by the Newton's law of
 149 cooling:

$$150 \quad q = hA(T_s - T_f) \quad (5)$$

151 where q is the heat flow between the body surface and the fluid, A the body surface in
 152 contact with the fluid, h the thermal convection coefficient and T_s and T_f are the absolute body
 153 surface and fluid temperatures, respectively. On the basis of the fluid motion, the convection
 154 may be classified as free (or natural) or forced. In the forced case, an artificially-induced
 155 convection current is created when a fluid is forced to flow around the body surface by means
 156 of an external source, such as a pump. In the case of natural convection, an increase of the
 157 temperature produces a reduction in the fluid density, which in turn causes the fluid motion.

158 In the system under study, the oven operates in vacuum and the convection contribution
 159 to the heat transfer is negligible.

160 4.3 Radiation

161 The thermal energy between two bodies is also exchanged through electromagnetic
 162 radiation. This mechanism is known as thermal radiation, because the random movement of
 163 atoms and molecules in a body, composed of charged particles, results in the emission of
 164 electromagnetic waves, which carry energy away from the body surface. Unlike convection,
 165 thermal radiation occurs also under vacuum. The transfer of radiant energy is described by the
 166 Stefan-Boltzmann's equation, which for two grey-body surfaces can be written as follows:

$$167 \quad Q = \frac{\sigma \cdot (T_1^4 - T_2^4)}{\frac{1-\epsilon_1}{A_1 \cdot \epsilon_1} + \frac{1}{A_1 \cdot F_{1 \rightarrow 2}} + \frac{1-\epsilon_2}{A_2 \cdot \epsilon_2}} \quad (6)$$

168 where:

169 Q is the heat flux;

170 σ is the Stefan-Boltzmann constant;

171 $\epsilon_{1,2}$ are the emissivities of the surfaces 1 and 2 (equal to 1 for a black body);

172 $A_{1,2}$ are the surface areas 1 and 2;

173 $F_{1 \rightarrow 2}$ is the shape factor;

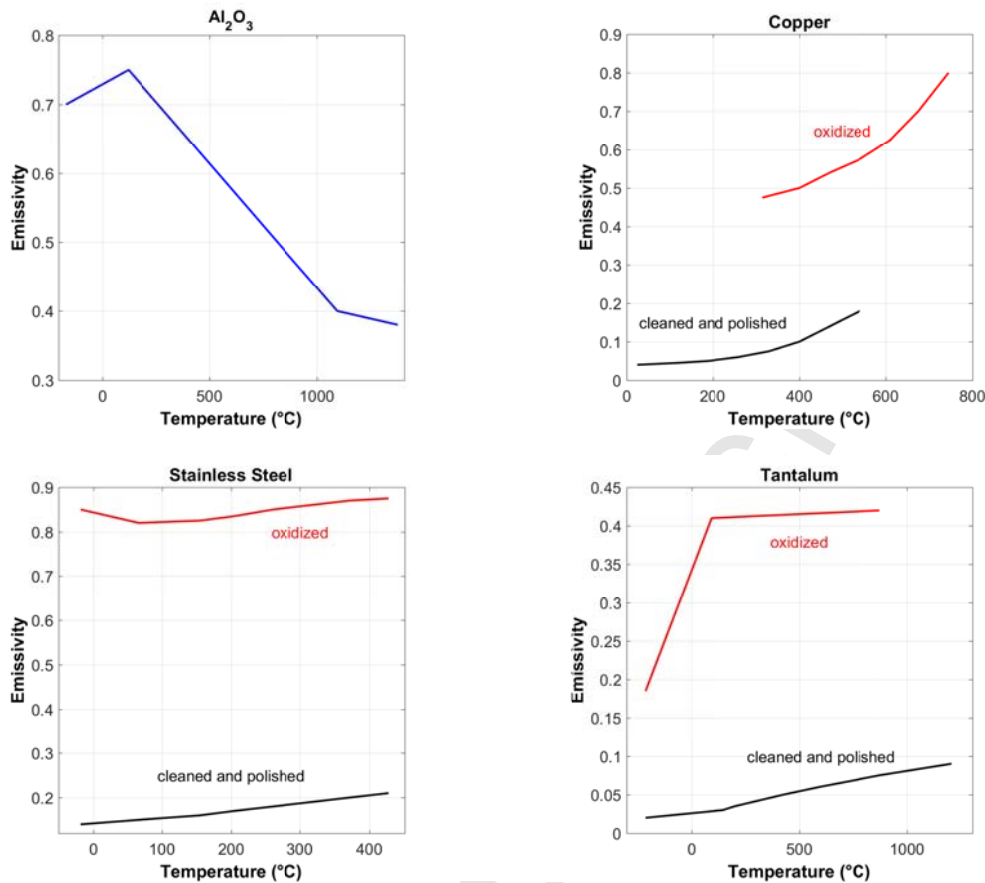
174 $T_{1,2}$ are the absolute temperatures in Kelvin of surfaces 1 and 2.

175 In (6), only the emissivity depends on the material, while the other parameters are
 176 constant or depend on the geometry. The emissivity represents the material effectiveness in
 177 emitting thermal radiation and is generally measured as the ratio of the thermal radiation from
 178 a surface to the radiation from an ideal black body surface at the same temperature. The ratio
 179 varies from 0 to 1. Kirchhoff's law equates the emissivity of an opaque surface with its

180 absorption of incident radiation. The largest absorptivity corresponds to complete absorption
181 of all incident light by a truly black object, explaining why mirror-like and polished metallic
182 surfaces that reflect light will thus have low emissivity. For several applications, when
183 conduction and convection are present, radiation becomes relevant only at high temperatures.
184 In the case under examination, radiation actually is the most relevant mechanism of heat
185 exchange also at low temperatures, given the absence of the convection contribution and the
186 low contact pressure between most of the components in contact, which minimizes the
187 thermal exchange by conduction (see section 6.3).

188 5. Materials

189 As seen in section 4, the heat flow and the temperature gradient in steady-state conditions
190 of the problem under study depend on the thermal conductivity and the emissivity of the
191 materials. These properties are temperature-dependent, and available in literature for all the
192 materials adopted in the analysis [9-11]. The emissivity, on the other hand, is strictly related to
193 the surface state of the radiating bodies [10]. Fig. 8 shows the emissivity values for alumina,
194 copper, stainless steel and tantalum as a function of temperature and surface state. It is
195 important to underline that in the numerical analysis the data is linearly extrapolated for the
196 higher temperatures. It is evident that, in general, the surface state consistently influences the
197 emissivity. Nevertheless, the surface state can be challenging to assess accurately considering
198 that it usually changes with time. The metal parts of the oven are machined without applying a
199 finishing polishing and are then operated at high temperatures in a residual gas atmosphere with
200 always some low level oxygen residue. Therefore, the surface conditions of the materials are
201 expected to be between the polished and oxidized limits.



202

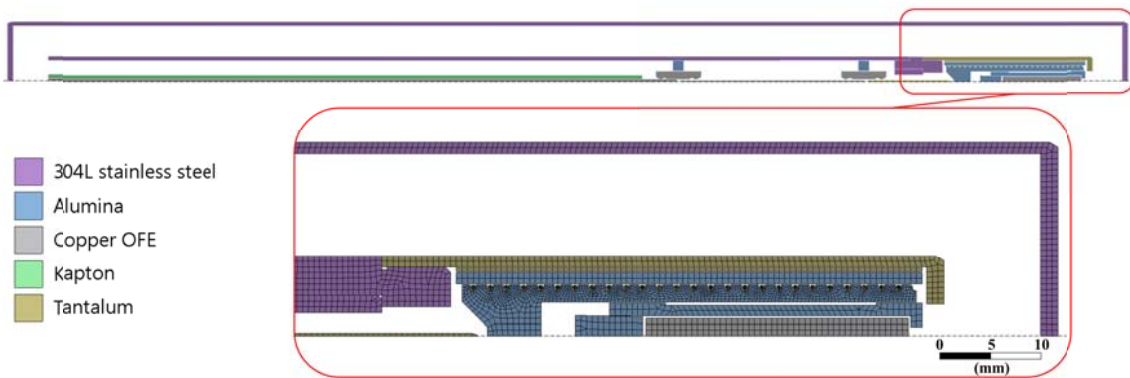
203

204 Figure 8 Emissivity vs. temperature as a function of the surface state for: *top left*) alumina
 205 (Al_2O_3), *top right*) copper, *bottom left*) stainless steel and *bottom right*) tantalum
 206 [[10](#),[11](#)].

207 6. Numerical model

208 6.1 Boundary conditions

209 Given the complex nature and nonlinearities of the problem, a finite-elements approach
 210 was adopted to model the system and the calculation was performed with ANSYS Workbench
 211 17.2. In the simulation, the oven geometry was reproduced with a 2D-axisymmetric model
 212 and the cane length reduced to 250 mm, which is the length contained in the vacuum
 213 enclosure of the off-line test stand. Room temperature was imposed at the end of the stainless
 214 steel cane, as measured at the vacuum seal during oven heating. In addition, an external frame
 215 was created at 10 mm radial distance from the oven which directly exchanges heat with the
 216 surrounding ambient at the constant temperature of 22 °C, [Fig. 9](#). It is important to highlight
 217 that the vacuum enclosure of the off-line test stand is roughly 50 mm around the oven;
 218 nevertheless, although the external frame in the model is much closer to the oven, the
 219 numerical results did not show significant difference moving it from 50 to 10 mm. The
 220 distance was set at 10 mm resulting in decreased calculation times.

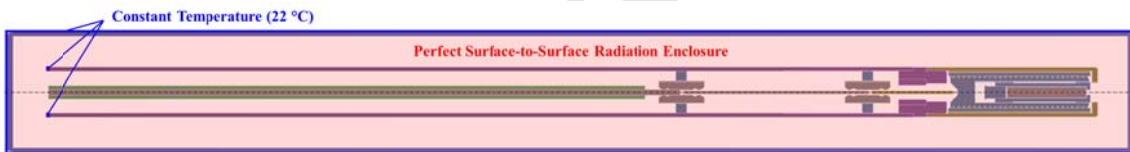


221

222

Figure 9 2D-axisymmetric model and materials.

223 The heat transfer between the components was modelled imposing a perfect surface-to-
 224 surface radiation, i.e. the total amount of energy exchanged inside a defined enclosure. In this
 225 case, the perfect enclosure is the whole area inside the simplified external frame, where
 226 surface-to-surface radiation occurs between the main system elements. In such enclosure the
 227 net total radiation is zero. The emissivity was imposed to the materials as a non-linear
 228 function of the temperature, according to the data from literature (Fig. 8). The boundary
 229 conditions are summarized in Fig. 10. Finally, the convection contribution was neglected for
 230 the reasons mentioned in section 4, while the conduction through the thermal interfaces was
 231 estimated according to (3) (see section 6.3).



232

233

Figure 10 Boundary conditions of the model.

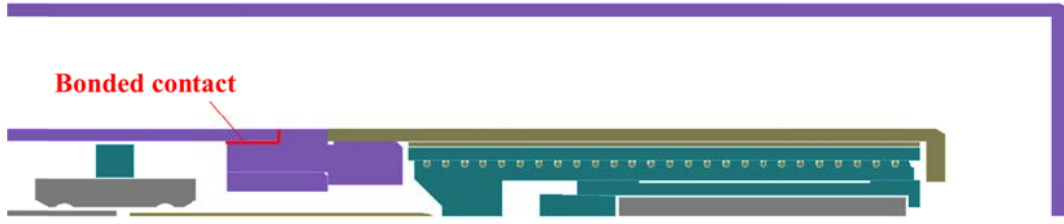
234 6.2 Mesh

235 The model features about 7000 plane elements and the minimum edge length is 35 μm
 236 for elements in the filament region. For meshing, the *PLANE77* element of ANSYS was used,
 237 which is an 8-node thermal element with one degree of freedom at each node. Moreover, this
 238 element is well suited to model curved boundaries because quad/triangular-shaped elements
 239 may be formed. The mesh quality assessment was performed investigating the element quality
 240 function, which provides a composite quality metric that ranges between 0 and 1. This metric
 241 is based on the ratio of the volume to the sum of the square of the edge lengths for 2D
 242 elements. A value of 1 indicates a perfect square while 0 indicates that the element has zero or
 243 negative volume. In the present model, the element quality is over 0.9 for more than 6500
 244 elements, i.e. 93% of the total.

245 6.3 Contacts

246 For most of the components in contact inside the oven, the pressure at the interfaces is
 247 very low and the body-to-body conductive heat transfer can be considered negligible with
 248 respect to the radiative one. Indeed, as shown in (4), for a low contact pressure the thermal
 249 conductance coefficient, h_c , approaches zero and, consequently, according to (3), the
 250 conductive heat flow approaches zero. The contact pressures were calculated considering the
 251 deadweight of the components. Nevertheless, in all cases, the thermal conductance coefficient
 252 is almost negligible (less than $0.1 \text{ Wm}^{-2}\text{K}^{-1}$), except for the oven-to-cane bolted connection in
 253 stainless steel (see Fig. 11), for which a thermal conductance coefficient of $14500 \text{ Wm}^{-2}\text{K}^{-1}$

254 was calculated assuming a tightening torque of 2 Nm, which corresponds to 1 kN of axial
 255 force, between the two components with M12 thread.



256

257

Figure 11 Oven-to-cane bonded contact.

258 6.4 Thermal loads

259 In normal operation the oven heating power is limited to 20 W and, based on the resistive
 260 power losses, one can estimate the power distribution in the different conductors (Tantalum
 261 (Ta), Copper (Cu) and stainless steel (SS)) as follows:

$$262 \text{ Power ratio} = \frac{P_i}{P_{tot}} = \frac{P_i}{P_{Ta} + P_{Cu} + P_{SS}} \quad (7)$$

263 where:

$$264 P = R \cdot I^2 = \frac{\rho \cdot l}{A} \cdot I^2 \quad (8)$$

265 P_i is either P_{Ta} , P_{Cu} or P_{SS} , while I is the current flowing through the conductors, as it is
 266 the same through all of them and thus disappears from the equation, the power ratios can be
 267 calculated. The conductors in the oven are: the tantalum filament, the copper wire inside the
 268 cane and the stainless steel cane which acts as a return conductor for current circuit.

269

Table 1: Power distribution ratios.

Conductor	Length l (mm)	Resistivity ρ ($n\Omega \cdot m$)	Cross section A (mm^2)	Power ratio
Ta filament	700	131	0.159	0.952
Cu wire	760	16.78	0.785	0.027
SS cane	760	690	40.84	0.021

270 The rough estimation of the power distribution reported in [Table 1](#) does not take into
 271 account the resistivity dependence with the temperature, but considers constant values at room
 272 temperature. On the other hand, most of the contribution to the total power comes from the
 273 tantalum filament, which results to it being the most heated and affected by the temperature
 274 increase. Taking into account that the resistivity usually increases as a function of the
 275 temperature, the relative contribution of tantalum to the total power would slightly further
 276 increase, approaching a value of 1. The error in the assumption of constant electrical resistivity
 277 with temperature is therefore less than 5%.

278 Considering the power distribution ratios in [Table 1](#), the power is applied in the model as
 279 an internal heat generation (IHG) to each component. Six different thermal analyses were
 280 performed, with power varying from 1 to 20 W; the power has been distributed in the
 281 conductors as reported in [Table 2](#).

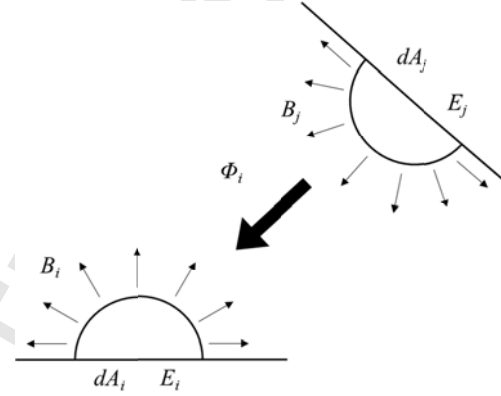
282

Table 2: Power distribution in the conductors.

Conductor	Volume (mm ³)	Total power (W)					
		1	2.5	5	10	15	20
		Distributed power (W)					
Ta filament	112.4	0.952	2.380	4.760	9.520	14.280	19.040
Cu wire	270.1	0.021	0.053	0.106	0.212	0.318	0.424
SS cane	11728.4	0.027	0.067	0.134	0.268	0.402	0.536

283 6.5 Solution algorithm

284 It is of interest to detail the numerical method adopted by the finite element code to solve
 285 the thermal problem. As described above, the thermal radiation is the main heat transfer
 286 mechanism between different bodies. Radiation analyses are highly nonlinear, with the flux
 287 varying with the fourth power of the body's absolute temperature, as seen in Eq. 6, and the
 288 iterative solution is based on a convergence criterion. The *radiosity solver method* is well suited
 289 for generalized radiation problems in 2D/3D involving two or more radiating surfaces. In
 290 ANSYS, this method can be used for either transient or steady-state thermal analyses. The
 291 radiosity solver method is based on the heat exchange between radiating bodies by solving for
 292 the outgoing radiative flux for each surface, when the surface temperatures for all surfaces are
 293 known. Considering two radiating surfaces i and j , Fig. 12, the energy leaving the unit area dA
 294 in all directions is B , therefore the total energy leaving the surface i ($B_i \cdot dA_i$) can be divided
 295 into its own radiant component and the diffuse reflection of the radiance coming from other
 296 surfaces.



297

298

Figure 12 Heat exchange between radiating bodies.

299 The total radiant energy corresponds to (6), simplifying the emission density E_i multiplied
 300 by the unit area ($E_i \cdot dA_i$). The diffuse reflection is the multiplication of the diffuse coefficient
 301 Φ_i and the part of energy coming from other surfaces which reaches the surface i . Integrating
 302 the contribution of all surfaces, the formula of the radiosity of the surface i is the following:

303

$$B_i \cdot dA_i = E_i \cdot dA_i + \Phi_i \cdot \int B_j \cdot F_{ji} \cdot dA_j \quad (9)$$

304 Where F_{ij} is the shape factor which determines the fraction of total energy leaving the
 305 surface j which reaches the surface i . The surface fluxes provide boundary conditions to the
 306 finite element model for the conduction process analysis. The heat conduction is governed by
 307 Fourier's law (1) and for steady state problems the solution only requires the knowledge of the
 308 thermal conductivity (2). When new surface temperatures are computed, due to either a new
 309 step or iteration cycle, new surface flux conditions are found by repeating the process. The

310 surface temperatures used in the computation must be uniform over each element surface facet
 311 to satisfy the conditions of the radiation model.

312 7. Results

313 In order to benchmark the experimental data, different simulations were run at increasing
 314 heating powers. While the thermal conductivity of the components as a function of temperature
 315 is well known from literature, the emissivity is the main variable affecting the thermal
 316 distribution. The range of values for the emissivity of each component was narrowed through
 317 bibliographic research, however, the emissivity strongly depends on the material surface state,
 318 which is unknown *a priori*. Parametric simulations were thus performed as a function of the
 319 different emissivities, to investigate the thermal response of the system.

320 7.1 Case 1

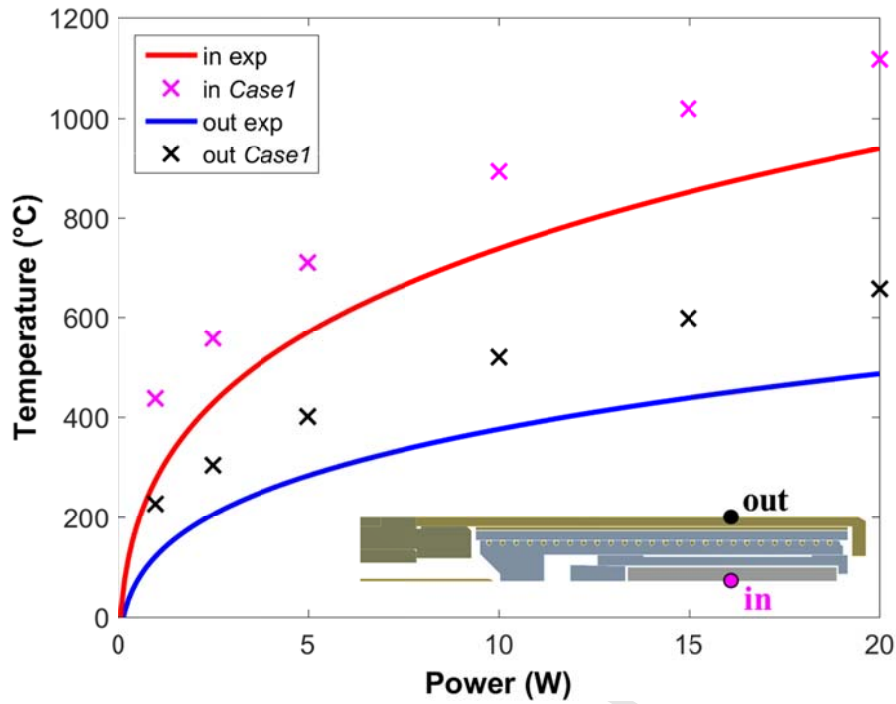
321 In the first case study (*Case 1*), the surface state was considered polished and cleaned for
 322 all the components. The emissivities used, extracted from [Fig. 8](#), are reported in [Table 3](#).

323 In [Fig. 13](#), the temperatures obtained experimentally and numerically at the probe
 324 positions are compared. It is possible to observe that the numerical results overestimate the
 325 temperature distribution inside and outside the oven.

326 Table 3: Material emissivities for *Case 1* [[10,11](#)].

Alumina		Tantalum		Stainless Steel		Copper	
$T (^{\circ}C)$	ϵ	$T (^{\circ}C)$	ϵ	$T (^{\circ}C)$	ϵ	$T (^{\circ}C)$	ϵ
-167	0.700	-212	0.020	-18	0.140	25	0.040
121	0.750	149	0.030	65	0.150	120	0.045
260	0.700	204	0.035	154	0.160	260	0.060
538	0.600	427	0.050	204	0.170	330	0.075
815	0.500	593	0.060	260	0.180	400	0.100
1093	0.400	871	0.075	316	0.190	470	0.140
1371	0.380	1204	0.090	427	0.210	540	0.180

327



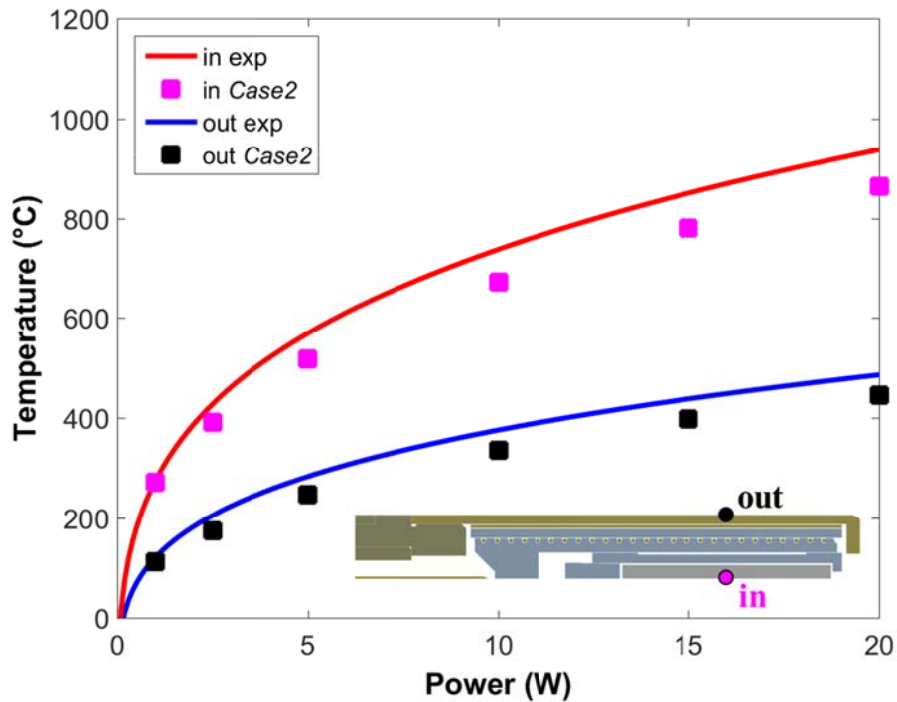
328

329

Figure 13 Numerical-experimental comparison for *Case 1*.

330 7.2 Case 2

331 As opposed to *Case 1*, *Case 2* assumes heavily oxidized surfaces. The numerical results
 332 are much closer to the experimental measures, [Fig. 14](#). The emissivities adopted are reported in
 333 [Table 4](#).



334

335

Figure 14 Numerical-experimental comparison for *Case 2*.

336

337

Table 4: Material emissivities for *Case 2* [10,11].

Alumina		Tantalum		Stainless Steel		Copper	
$T (^{\circ}C)$	ϵ	$T (^{\circ}C)$	ϵ	$T (^{\circ}C)$	ϵ	$T (^{\circ}C)$	ϵ
-167	0.700	-212	0.185	-18	0.850	315	0.475
121	0.750	93	0.410	65	0.820	400	0.500
260	0.700	871	0.420	154	0.825	470	0.540
538	0.600			204	0.835	540	0.575
815	0.500			260	0.850	610	0.625
1093	0.400			316	0.860	675	0.700
1371	0.380			427	0.875	745	0.800

338 The real scenario lays between the two extremes, *Case 1* and *Case 2*. In fact, even if the
 339 initial surface state of the components is measurable, the level of oxidation changes with time
 340 and heating cycles. Several simulations were performed with different emissivity values for the
 341 materials, depending on the different oxidation levels assumed. Sensitivity analyses showed
 342 that the results were mostly sensitive to the variation of the emissivity of tantalum. Out of the
 343 tens of different combinations simulated, two additional cases to *Case 1* and *Case 2* are
 344 reported in this work.

345 7.3 Case 3 and 4

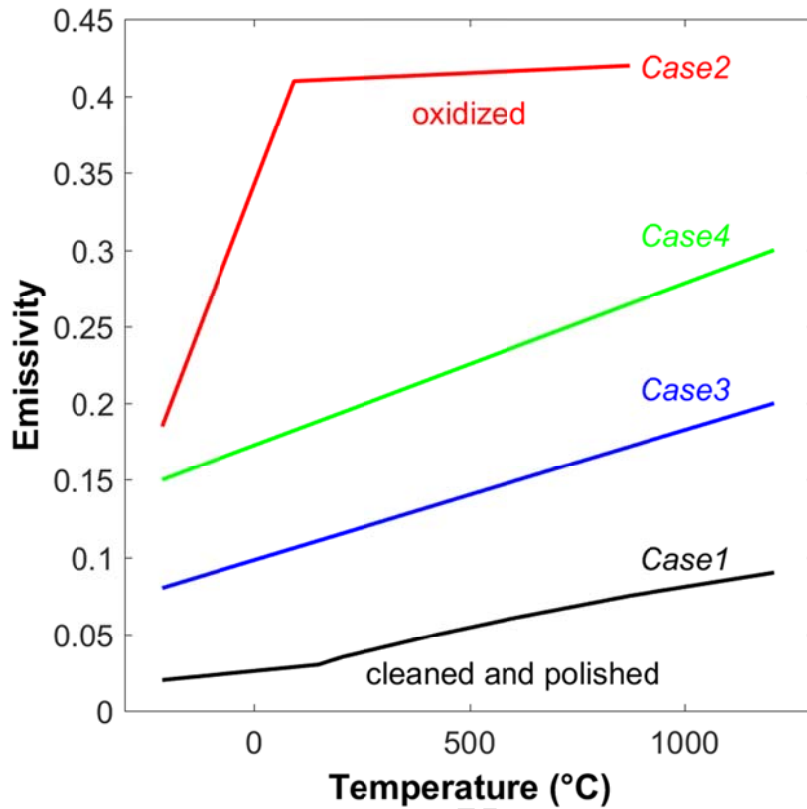
346 Section 7.2, and in particular *Case 2*, shows that the assumption of oxidized materials
 347 well represents the behaviour of the oven in operation. While the exact grade of oxidation of
 348 the components is uncertain, one can deduce, looking at [Fig. 14](#), that it is lower than what
 349 assumed in *Case 2*. A fine-tuning of *Case 2* was therefore performed in terms of emissivity of
 350 the tantalum, which resulted, out of the sensitivity study performed, the most influent parameter
 351 in the determination of the results. Two additional cases, with intermediate tantalum oxidation,
 352 *Case 3* and *Case 4*, were run. For the new cases, a simple linear relationship between emissivity
 353 and temperature was assumed. The tantalum emissivities used in the four cases are reported in
 354 [Table 5](#) and, for the sake of clarity, their difference is graphically shown in [Fig. 15](#).

355

Table 5: Tantalum emissivities for different cases simulated.

Case 1		Case 2		Case 3		Case 4	
$T (^{\circ}C)$	ϵ	$T (^{\circ}C)$	ϵ	$T (^{\circ}C)$	ϵ	$T (^{\circ}C)$	ϵ
-212	0.020	-212	0.185	-212	0.080	-212	0.150
149	0.030	93	0.410	1204	0.200	1204	0.300
204	0.035	871	0.420				
427	0.050						
593	0.060						
871	0.075						
1204	0.090						

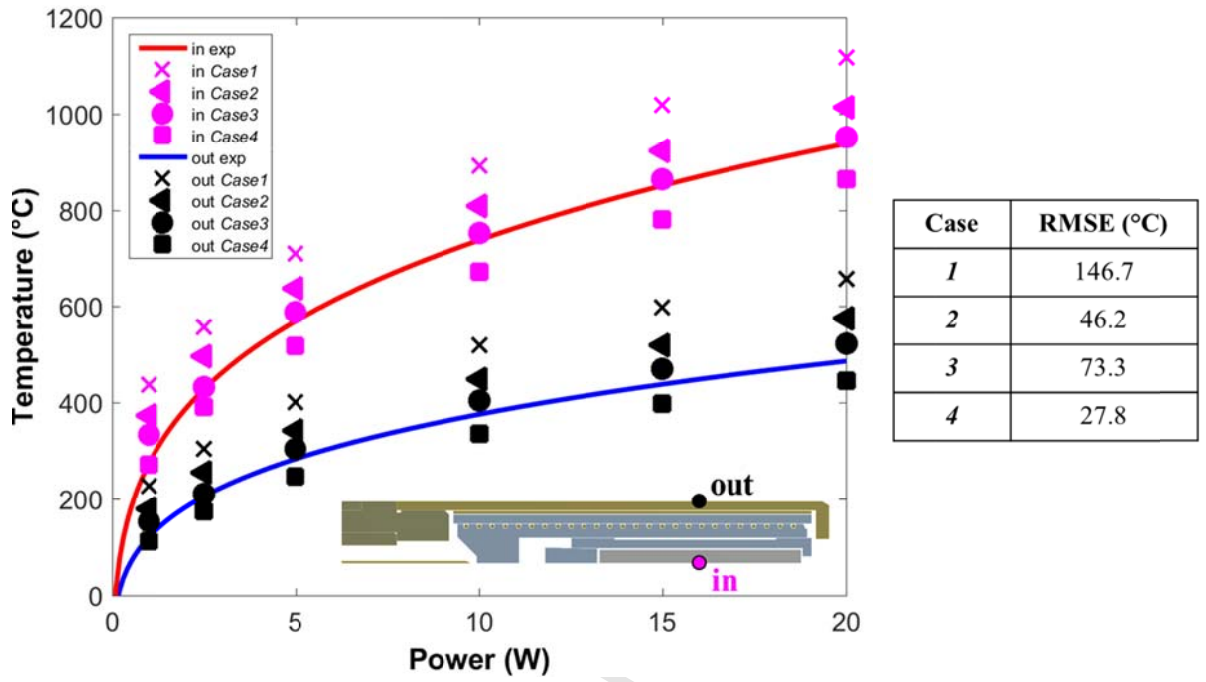
356



357

358 Figure 15 Emissivity vs. temperature for tantalum in the different cases simulated.

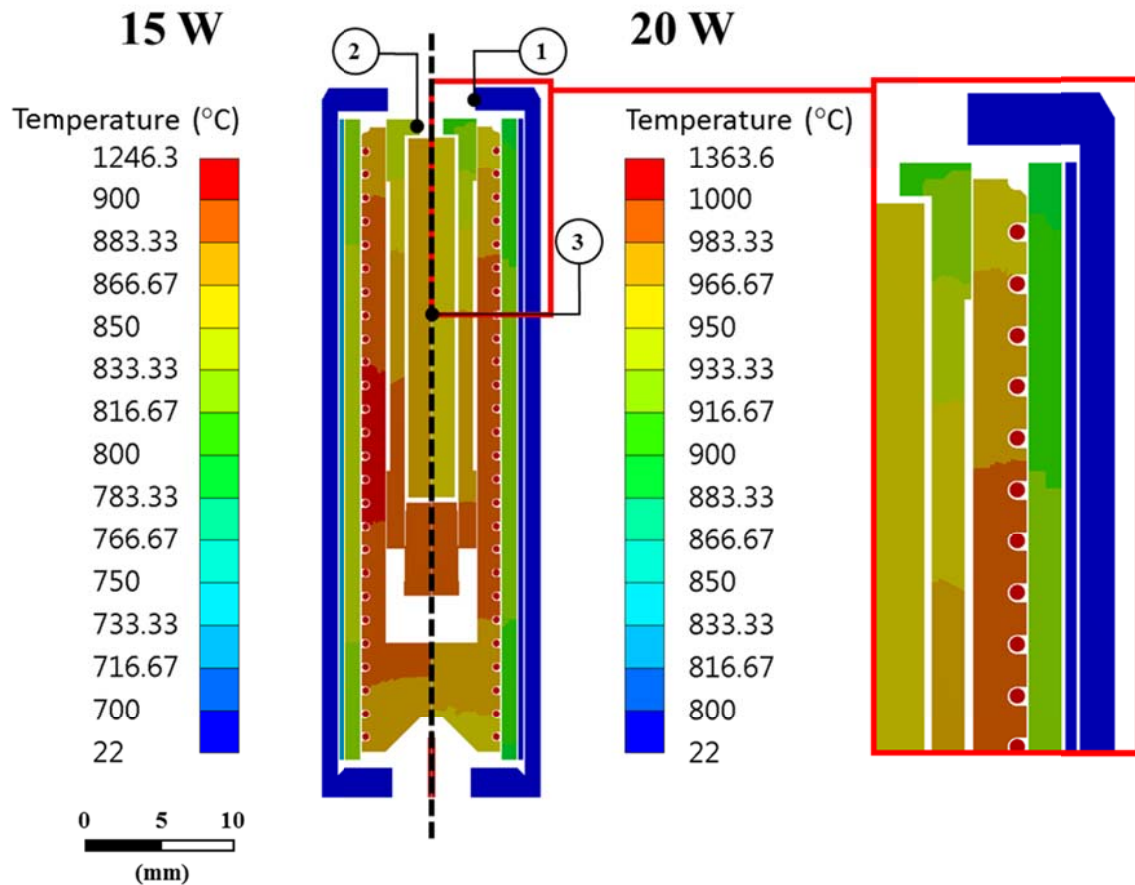
359 The results with the new ranges of the tantalum emissivity are shown in [Fig. 16](#). In
 360 addition, the root-mean-square error (RMSE) for each case is reported in order to estimate the
 361 differences between the simulated results and the experimental measures. *Case 4* shows the
 362 best agreement with the experimental data. This scenario features an intermediate oxidation of
 363 tantalum which is also compatible with the visual inspections performed on the component.



364

365

Figure 16 Numerical-experimental comparison for cases 1 to 4.

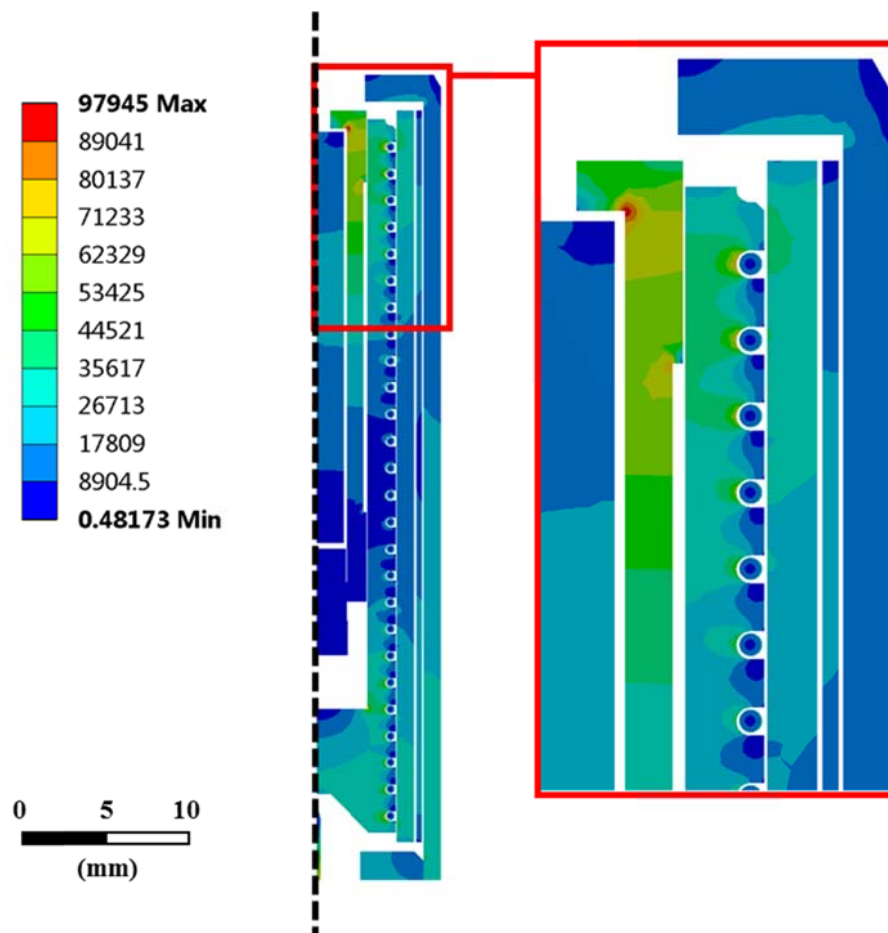


366

367 Figure 17 *Case 4* model: simulated temperature distribution inside the GTS-LHC miniature
 368 oven with 15 and 20 W heating powers. The oven tip is at the top. Temperatures at
 369 locations 1, 2 and 3 are 482, 834 and 870 °C for the 15 W case and 536, 915 and
 370 960 °C for the 20 W case.

371

372 [Fig. 17](#) presents the calculated temperature distributions inside the oven with 15 W and
 373 20 W heating powers. It is possible to observe that a rather good temperature uniformity is
 374 achieved along the crucible, while the tip of the oven remains significantly colder. At 20 W
 375 the temperature gradient between the material in the crucible (point 3) and the crucible tip
 376 (point 2) is about 45 °C, while between the crucible tip and the oven tip (point 1) it is about
 377 420 °C. This relevant gradient between the inner and outer part of the oven can be further
 378 highlighted observing the heat flux in [Fig. 18](#). Indeed, the heat flux is concentrated between
 379 the filament, i.e. the heating source, and the crucible confining most of the energy around the
 380 copper pin.



381

382

Figure 18 *Case 4* model: heat flux (Wm^{-2}) at 20 W heating power.

383

8. System optimization

384

385

386

387

388

389

390

391

392

The tantalum emissivity was found to be the most important parameter influencing the behaviour of the system. Nevertheless, the emissivity depends on the surface state, which changes during time due to oxidation. This effect can be taken into consideration introducing a relationship between time and emissivity for tantalum. In order to do so, the emissivity should be measured at different working times in the test bench oven, predicting the behaviour of the component during operation in the ion source. Of course, this method is effective if the initial emissivity and surface state of the tantalum used in the test bench and in the source are the same. In that sense, surface treatments, such as sandblasting or ion bombardment, can be effectively performed to impose the desired surface state to the component [12].

393

394

395

396

397

398

399

400

401

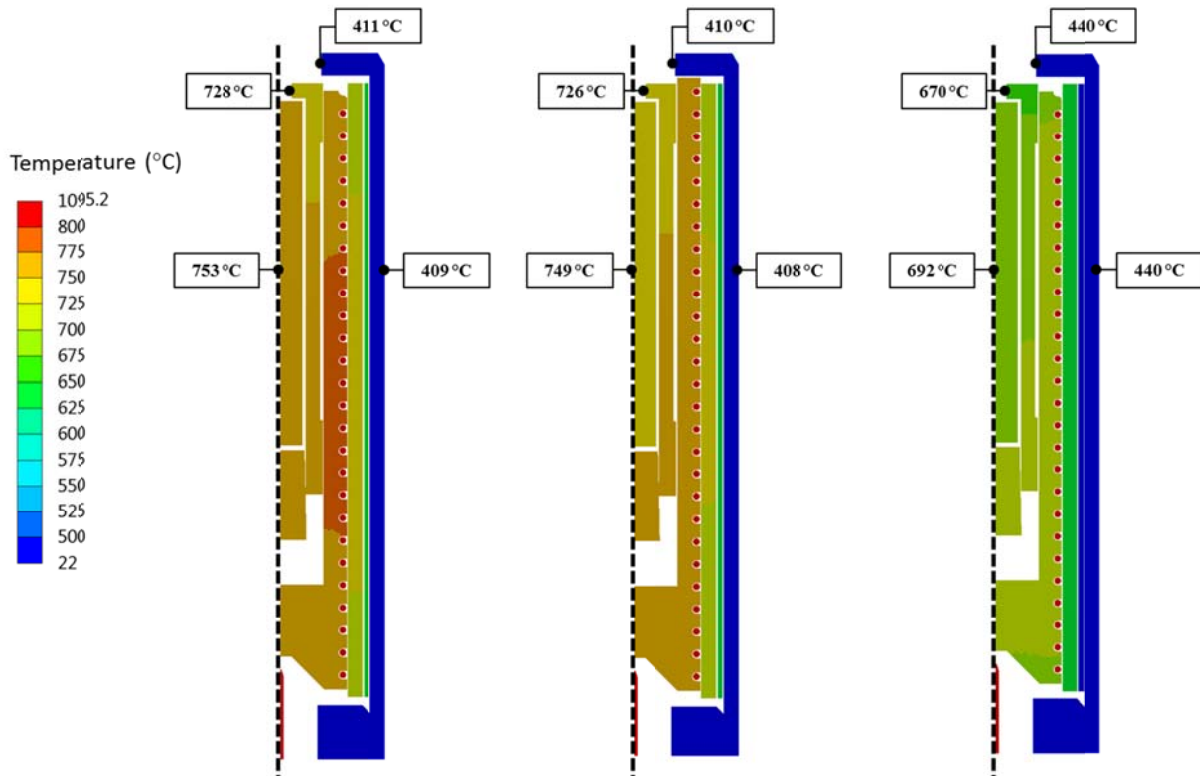
402

403

Moreover, the calculated temperature distribution inside the oven shows a good axial uniformity at different heating powers; nevertheless, the temperature drop in the oven tip has given the first hints to possible causes of the observed early reduction of the oven performance. Indeed, in normal operation the two ovens installed in the GTS-LHC provide 2-3 weeks of lead beam operation between refills. However, it was observed that when a refill is required due to degrading beam performance, typically about 2/3 of the lead is still left in the oven. In some cases the operation is also interrupted by blockage of the oven tip, either by formation of lead oxide or droplets of metallic lead which could be caused by the cold oven tip observed in the simulations. In order to reduce the temperature gradient in the oven tip, a possible solution could be to improve the filament winding around the crucible, exploiting all the available space, in particular close to the tip. Additionally, increasing the contact pressure between the

404 components would enhance the heat transfer by conduction, facilitating the thermal diffusion
 405 and reducing the temperature gradients between the oven parts.

406 The effectiveness of these two last proposals was analysed by means of numerical simulations.
 407 Concerning the filament winding, the oven geometry was modified extending the filament
 408 support in order to exploit all the free space close to the oven tip (Fig. 19 *centre*). Instead, the
 409 enhancement of the thermal diffusion by conduction was simulated setting a perfect contact
 410 between the tantalum reflector foil and the oven cover. In Fig. 19 the temperature distribution
 411 obtained at 10 W in these two cases is compared with what obtained with the baseline of
 412 *Case 4*.



413
 414 Figure 19 Temperature distribution of different numerical simulations at 10 W oven power:
 415 *left*) actual oven geometry radiation dominated, *centre*) modified geometry
 416 exploiting the available space close to the oven tip and *right*) actual oven geometry
 417 with the tantalum reflector foil in contact with the oven cover.

418 The comparison shows that the extension of the filament support up to the tantalum cover
 419 slightly modifies its temperature distribution with respect the original oven geometry. However,
 420 this solution has no relevant effect on temperature along the crucible and, in particular, on the
 421 temperature gradient in the oven tip, which is about 315 °C as in the baseline case. On the other
 422 side, enhancing the thermal conduction between the reflector foil and the oven cover has a
 423 relevant influence on the thermal behaviour of the system. Indeed, the first evident result is the
 424 drop-off, by about 60 °C, of the temperature in the inner side of the oven; nevertheless, the
 425 temperature uniformity is maintained along the crucible. This effect is complemented by a
 426 temperature increase of about 30 °C in the tantalum cover due to the thermal diffusion between
 427 the reflector foil and the cover. The temperature gradient in the oven tip is reduced to 230 °C,
 428 30% less than the gradient of the baseline case.

429 9. Conclusions

430 An advanced numerical study was performed with the finite-elements method to evaluate
431 the temperature distribution in the miniature ovens installed in the Linac3 GTS-LHC ECR ion
432 source and assess the thermal behaviour of the system, which strongly influences the
433 operational performance of the component. The thermal radiation was determined to be the
434 main contribution to the heat exchange between the oven parts. The numerical model was
435 benchmarked with measurements taken in an offline test stand which reproduces the same
436 environment and thermal system of the ion source. The numerical simulations provided good
437 agreement with the experimental data and, analysing the results, the tantalum emissivity turned
438 out to be the crucial parameter influencing the behaviour of the system. Since the emissivity
439 depends on the surface state, a satisfactory numerical-experimental benchmarking was obtained
440 assuming intermediate conditions in terms of tantalum oxidation. Proposals to improve the
441 thermal performance of the system were discussed considering the experimental observations
442 and numerical outcome. Numerical simulations shown that introducing the thermal conduction
443 between bodies allows to improve the temperature distribution of the system and, consequently,
444 the service life of the source. Finally, the results obtained allowed to pinpoint general
445 guidelines which could be beneficial also for similar systems and technologies. First of all, it is
446 fundamental to assess and control the surface state of the components at the beginning of their
447 life, and evaluate the evolution of the oxidation of the equipment during operation. Moreover,
448 the emissivity of the adopted materials has to be carefully measured as a function of the surface
449 state and oxidation on material samples. Finally, in order to obtain a more accurate model
450 validation and monitor the temperature gradients along the structure components, the data
451 acquisition system in dedicated test benches should feature an increased number of measuring
452 points.

453 References

- 454 [1] G. Apollinari et al., “High-Luminosity Large Hardon Collider (HL-LHC): Preliminary
455 Design Report”, Rep. CERN, CERN-2015-005, 2015.
- 456 [2] H.D. Haseroth, “Pb injector at CERN”, Conf. Proc. C9608262, vol.1, pp.283-287, 1996.
- 457 [3] L. Dumas et al., “Operation of the GTS-LHC Source for the Hadron Injector at CERN”,
458 in Proc. of ECRIS 2006, Lanzhou, China, published in HEP & NP, Vol.31, Suppl.1, pp.51-54
459 (2007). Also available as LHC Project Report 985.
- 460 [4] V. Toivanen et al., “Effect of double frequency heating on the lead afterglow beam
461 currents of an electron cyclotron resonance ion source”, Physical Review Accelerators and
462 Beams 20, 103402, 2017.
- 463 [5] V. Toivanen et al., “Recent developments with the GTS-LHC ECR ion source at CERN”,
464 in Proc. of ECRIS 2016, Busan, Korea.
- 465 [6] ANSYS Workbench User’s Guide, Release 15.0, 2013.
- 466 [7] E.E. Marotta et al., “Thermal joint resistance of polymer-metal rough interfaces”, J. of
467 Electronic Packaging, Vol.128, pp.23-29, 2006.
- 468 [8] M.G. Cooper et al., “Thermal contact conductance”, Int. J. Heat Mass Transfer, Vol.12,
469 pp. 279-300, 1969.

- 470 [9] J.H. Lienhard IV, J.H. Lienhard V, "A heat transfer textbook", 4th Edition, Phlogiston
471 Press, 2016.
- 472 [10] W.D. Wood et al., "Thermal radiative properties", No. 3, Plenum Press Handbooks of
473 High-Temperature Materials, 1964.
- 474 [11] E.A. Avallone and T. Baumeister III, "Marks' Standard Handbook for Mechanical
475 Engineers", McGraw-Hill, New York, NY, pp.63-79, 1978.
- 476 [12] Z. Sobiech et al., "Cooling of the LHC injection kicker magnet ferrite yoke:
477 measurements and future proposals", Proceeding of IPAC 2014, Dresden, Germany,
478 pp.544-546, 2014.